# RESEARCH ARTICLE





# Hydrodynamic interactions of filaments polymerizing against obstacles

# **Ehssan Nazockdast**

Department of Applied Physical Sciences, University of North Carolina, Chapel Hill, North Carolina

#### Correspondence

Ehssan Nazockdast, Department of Applied Physical Sciences, University of North Carolina, Chapel Hill, NC 27599. Email: ehssan@email.unc.edu

#### Abstract

Polymerization and depolymerization of cytoskeletal filaments against cellular structures can generate forces that are key to many cellular processes, such as cell motility and chromosomes movements during cell division. Motions generated by these forces induce global cytoplasmic flows and couple the dynamics of the polymerizing filaments and other bodies immersed in the fluid through their long-range hydrodynamic interactions (HIs). Previous theoretical and computational studies have largely ignored HIs. We use three dimensional discrete simulations to study the relationship between polymerization forces and their resulting flows and Hls. As a model system, we choose a filament that is polymerizing against an obstacle, and is embedded in a cylindrical array of parallel filaments of the same length. We consider three distinct mechanical scenarios for the filaments within the array: (a) all of the filaments are polymerizing with the same velocity; (b) they are all fixed in space, and (c) they are freely suspended. We show that each of these conditions produce their unique cytoplasmic flows and each result in differentiable polymerization forces and velocities. We also study the effect of buckling of filaments on polymerization forces and velocities and discuss the effect of HIs on the onset of buckling transition. Finally, we show that HIs result in the bundling of the buckled filaments within the array.

## **KEYWORDS**

buckling instability, force-velocity relationship, hydrodynamic interactions, polymerization forces

# 1 | INTRODUCTION

Polymerization and depolymerization of cytoskeletal filaments can generate forces in the absence of molecular motors (Howard, 2001; Mogilner, 2006). These forces are involved in many cellular motions, such as cell's crawling motion driven by actin polymerization (Bray, 2000), as well as the motion of chromosomes (Joglekar, Bloom, & Salmon, 2010) and the spindle positioning and assembly (Garzon-Coral, Fantana, & Howard, 2016; Oriola, Needleman, & Brugués, 2018) during cell division, that depend on polymerization and depolymerization of microtubules. The polymerization forces have been experimentally measured in-vitro for both microtubules (Dogterom &

Yurke, 1997) and actin filaments (Footer, Kerssemakers, Theriot, & Dogterom, 2007).

Large number of theoretical studies have focused on the mechanisms of force generation. The first mechanistic theory was proposed by Peskin, Odell, and Oster (1993) for force generation by a polymerizing filament against an obstacle. In their *Brownian ratchet model*, a rigid filament polymerizes perpendicular to the surface of an obstacle. The polymerization rectifies the diffusive motion of the obstacle, which results in an effective pushing force that moves the obstacle in the direction of polymerization. For the polymerization to continue, the Brownian fluctuations of the obstacle must open a gap large enough to intercalate a monomer. Mogilner and Oster (1996) extended the formulation to

586 © 2019 Wiley Periodicals, Inc. wileyonlinelibrary.com/journal/cm Cytoskeleton. 2019;76:586–599.

flexible filaments and proposed elastic Brownian ratchet mechanism. where the polymerization gap is generated by thermal bending undulations of the filaments. These theories have since been extended to accommodate other experimental observations. These include theories for filaments with multiple crosslinked protofilaments such as microtubules (van Doorn, Tănase, Mulder, & Dogterom, 2000), and theories that include interactions with filament end-tracking proteins (Dickinson, Caro, & Purich, 2004); see Holz and Vavylonis (2018) and Mogilner (2006) and the references within for reviews on the topic. The interactions included in these theories are local that is, they occur over the length-scales of monomers and protein structures, which are significantly smaller than the length of the filaments. The final result of each of these theories is a relationship between the applied pushing force to the obstacle and the filament's polymerization velocity that is, force-velocity relationship. Finding a force-velocity relationship is not the subject of this work. Instead, we assume a force-velocity relationship is provided to us by experiments and theories.

In most physiological conditions, the cytoskeletal filaments exchange forces with motor-proteins and crosslinkers, leading to a complex range of structures and rheological behavior. Examples include viscoelastic (Bausch & Kroy, 2006), poroelastic (Moeendarbary, Valon, Fritzsche, Harris, & Dale, 2013), active gel (Kruse, Joanny, Jülicher, Prost, & Sekimoto, 2005), and soft glassy behaviors (Fabry et al., 2001). In this study, to focus on the effect of HIs, we do not include these interactions. In this limit, the polymerization forces and velocities are fully determined once the force-velocity relationship is complimented with equations that balances the polymerization force against the drag force induced by pushing the filament (and/or obstacle in case of a mobile obstacle) through the fluid medium.

The motion of the filaments and obstacles generate global cytoplasmic flows in scales of the largest dimensions of the moving objects (Nazockdast, Rahimian, Needleman, & Shelley, 2017; Shelley, 2016). As a result, objects that are separated by distances as large as the filaments length interact with one another through these flows. These nonlocal interactions are referred to as hydrodynamic interactions (HIs), which play a key role in determining the drag force on the polymerizing filaments.

While previous discrete simulations have largely ignore HIs, there have been a number of continuum modeling studies that account for HIs and fluid-structure interactions; see Mogilner and Manhart (2018) and Shelley (2016) for comprehensive reviews on actin and microtubule assemblies, respectively. The main ingredients of these continuum two-phase models are the momentum and mass transfer for the cytoplasmic fluid and the filament phases and the mechanical coupling between them. The cytoplasm is typically modeled as a Newtonian fluid in Stokes flow, while—depending on the microstructural details such as crosslinking and motor activities—different models have been utilized for describing the mechanics of the filament phase. For example, some studies model the cytoskeleton as a poroviscous material (Cogan & Guy, 2010; Dembo & Harlow, 1986), and others use a poroelastic description (Bottino & Fauci, 1998; Strychalski, Copos, Lewis, & Guy, 2015; Strychalski & Guy, 2013, 2016). In these classes

of models, the coupling between the cytoplasm and the filament phase is typically modeled through a friction term that depends on their relative velocity. In many other studies the intracellular flows and the viscous forces on the filaments are ignored, and the cytoskeleton is modeled as an elastic gel (Bottino, Mogilner, Roberts, Stewart, & Oster, 2002; Marcy, Prost, Carlier, & Sykes, 2004; Plastino & Sykes, 2005). Another class of theories models the mixture of the cytoplasm and its embedded filaments and motors as an active gel (Brugués & Needleman, 2014; Kruse et al., 2005).

The main drawback of these continuum models is that the relationship between the micromechanical interactions of polymerizing filaments with motors and obstacles and the emergent macroscopic (continuum) behavior is not very clear. Thus, it becomes challenging to choose the correct continuum model and sets of parameters that describe a particular problem. Discrete simulations provide a natural pathway to overcome this difficulty. The aim of this work is to use discrete simulations to study how HIs between polymerizing filaments and the surrounding cytoskeletal structures under different micromechanical conditions can change the polymerization forces and velocities.

Computational methods for simulating cytoskeletal filaments in fluid medium can be divided into volume-based and particle-based methods. In volume-based methods, the momentum equation in the fluid domain (Stokes or Navier-Stokes equations) are solved by discretizing the entire fluid volume and solving for the fluid velocity within the volume by imposing proper boundary conditions on the immersed bodies and outer boundaries. Within this group, immersed boundary method (IBM) has been used to simulate filaments (Lim & Peskin, 2012; Wiens & Stockie, 2015), and has been extended to include thermal fluctuations for applications to different cellular processes (Atzberger, Kramer, & Peskin, 2007). The most widely used particle-based method is the bead-spring model, where the filament is represented by the collections of rigid spheres connected by springs with bending stiffness, and varying degrees of extensional stiffness. While some implementations of this method include HIs (Joung, Phan-Thien, & Fan, 2001), most only include local drag on the beads and the rods connecting the beads (Nedelec & Foethke, 2007).

The method used in this study is based on slender-body theory (SBT) for filaments in Stokes flow, where the slenderness of the filament is used to asymptotically recast the solution to Stokes equation in terms of integrals of point-forces along the filament's centerline. These solutions are accurate to  $\mathcal{O}(\varepsilon^2 \text{log}\varepsilon)$ , where  $\varepsilon \ll 1$  is the aspect ratio of the filament(s) (Johnson, 1980; Keller & Rubinow, 1976). We have recently used SBT to develop a platform for large-scale simulations of cytoskeletal assemblies that explicitly accounts for HIs, as well as the filaments' flexibility, polymerization/depolymerization dynamics and interactions with molecular motors Nazockdast, Rahimian, Zorin, and Shelley (2017). A brief description of this platform is provided in Supporting Information.

We have previously used this method in studying the pronuclear positioning during the first cell division of *Caenorhabditis elegans*, which involves centering of the pronuclei and alignment of the microtubule organizing centers with anterior-posterior axis of the cell (Nazockdast, Rahimian, Needleman, & Shelley, 2017). One of the proposed mechanisms for spindle and pronuclei positioning is the cortical pushing model, where pushing forces are applied to the spindle and pronuclei by polymerization of astral microtubules against the cellular boundary. Figure 1 shows two snapshots of the pronuclei (modeled as a rigid sphere) and their attached astral microtubules during pronuclear migration in cortical pushing model, and the cytoplasmic flows generated by it. As shown in Figure 1b, even after the pronuclei are properly positioned and are stationary, strong flows are generated near the cellular boundaries by polymerization forces. One question that arises is: How are the polymerization forces and velocities influenced by interactions of polymerizing microtubules through the cytoplasmic flows they generate?

Understanding the precise role of HIs in determining polymerization forces in a problem such as pronuclear migration is very challenging, as it involves several parameters and geometrical complexities. Instead, we take a reductionist approach and choose the special case of a polymerizing filament embedded in a cylindrical array of parallel filaments of identical lengths. We assume that the filament is polymerizing from the end that is nearly touching the obstacle, while the other end is mechanically free and not polymerizing (inactive); see Figure 2a.

To draw clear contrasts between the effect of HIs in different mechanical conditions, we consider three scenarios with distinct HIs. In *Scenario I*, we assume the filaments within the array are all polymerizing against the obstacle with the same velocity. A few physiological conditions which closely resemble this condition are the polymerization and depolymerization of kinetochore microtubules against chromosomes in metaphase state (Joglekar, Bloom, & Salmon, 2010), (Tomographic reconstructions of the mitotic spindle structure show that kinetochore microtubules are not directly connected to the centrosomes in *C. elegans* and their minus-ends may be mechanically free (Redemann et al., 2017), while their plus-end is attached to the chromosomes) and the polymerization of a network of actin filaments against beads that are coated with proteins that promote Arpr2/3-mediated actin nucleation and polymerization (Cameron, Footer, Van Oudenaarden, &

Theriot, 1999; Marcy et al., 2004), as well as nucleation and processive assembly of actin filaments against beads that are coated with formin (Kovar & Pollard, 2004; Romero et al., 2004).

In *Scenario II*, the filaments inside the array are not polymerizing and are held fixed. Conditions similar to this scenario are the polymerization of microtubules against cell cortex in the presence of actin cytoskeletal network, or actin filaments polymerizing in the network of other crosslinked actin filaments.

A large fraction of filaments and organelles are freely suspended in the cytoplasm. How does the presence of these immersed bodies affect the mechanics of polymerizing filaments? We study this effect in *Scenario III*, where we assume the filaments within the array are freely suspended and inactive.

The outline of the paper is as follows. We begin in Section 2.1 by computationally studying the generated flows and the drag force on a *rigid* filament polymerizing within an array of rigid filaments in the three mentioned scenarios. In Section 2.1.1, we study how HIs in Scenarios I and II affect the polymerization velocities. In Section 2.2, we extend our analysis to flexible filaments; we study the buckling transition induced by pushing forces from polymerization of a single filament against an obstacle, and the effect of buckling on the polymerization velocity of a single filament. We then discuss the effects of HIs of an arrays of filaments on the buckling transition, and the resulting polymerization velocities in Sections 2.2.1 and 2.2.2. Finally, in Section 2.2.3, we show how HIs can lead to bundling of buckled polymerizing filaments.

# 2 | RESULTS

# 2.1 | Rigid polymerizing filaments

We start by studying the effect of HIs on polymerizing filaments, when the viscous forces are much smaller than elastic forces and filaments can be treated as rigid and straight. We consider an array of  $N_F = 20$  parallel rigid filaments of the same length. As shown in Figure 2b, the filaments ends are uniformly distributed over a surface

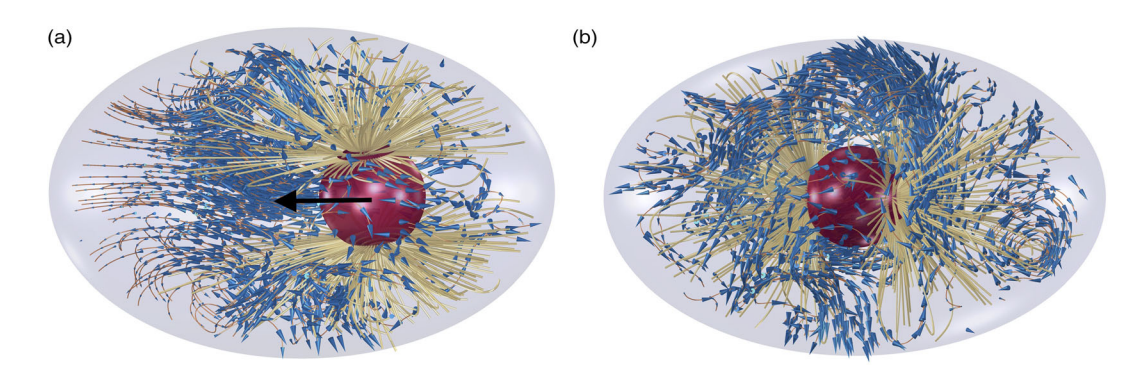


**FIGURE 1** Simulation snapshots of the pronuclei (red sphere) and their anchored astral microtubules (600 yellow filaments) migrating from the posterior pole of the cell (right side) to the anterior pole (left side), and the flow generated by the motion of this structure and the polymerization of microtubules against cellular boundaries. (a) The initial stage of migration, where the pronuclei are moving toward the center; (b) the later stage of migration, where the pronuclei are properly positioned [Color figure can be viewed at wileyonlinelibrary.com]

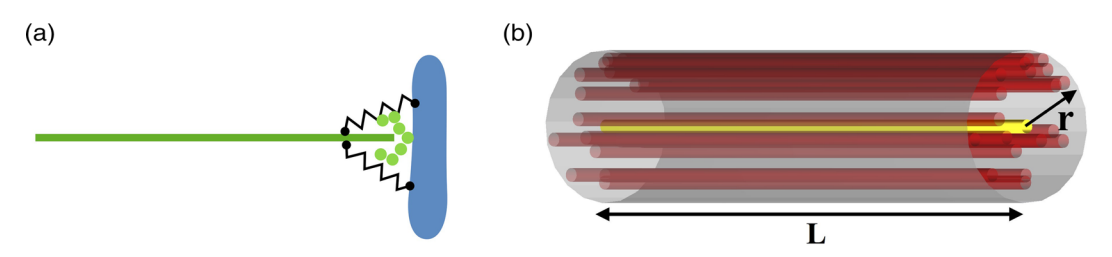


**FIGURE 2** (a) Schematic presentation of a filament polymerizing against an immobile obstacle from one end, while the other end is free and stable. (b) Schematic presentation of a polymerizing filament (yellow) of length *L* embedded in a cylindrical array of radius r, containing parallel filaments of the same length. The filaments within the array are (I) polymerizing with the same velocity as the filament, (II) fixed, and (III) freely suspended in space [Color figure can be viewed at wileyonlinelibrary.com]

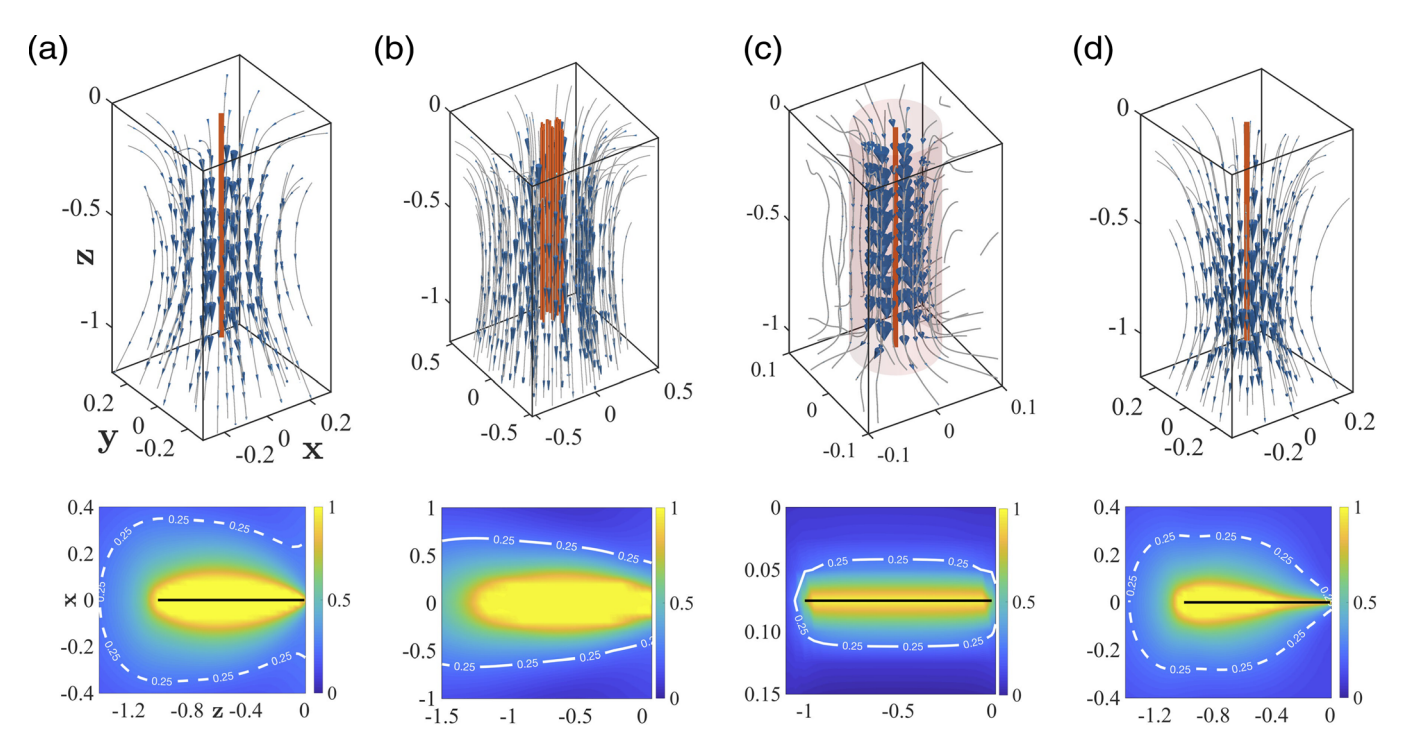


**FIGURE 3** Top panel: The 3D flows induced by the polymerization of filament(s) against an obstacle (z = 0 plane). (a) A single filament, (b) an array of 20 polymerizing filaments (Scenario I), (c) a single polymerizing filament embedded in an array of 20 fixed filaments (Scenario II), and (d) a single polymerizing filament embedded in an array of 20 freely suspended filaments (Scenario III). Bottom panel: the velocity magnitudes of those flows in z - x plane, made dimensionless by the magnitude of polymerization velocity. The polymerizing ends are located at z = 0. The dashed lines show the contours corresponding to velocity magnitude of 0.25. Note that the x-axis and y-axis limits are different in each figure. The polymerizing filaments are shown as solid black lines in the bottom panels, except for Figure 3b (20 filaments are polymerizing) for visualization purposes [Color figure can be viewed at wileyonlinelibrary.com]

of radius r where r/L=0.1. The filaments are *nearly touching* the obstacle from their polymerizing ends. For numerical tractability we assume the filament tip is separated from the obstacle by a small gap of size  $\delta=0.04$  L. The reason for this is explained in the description of the numerical platform provided in Supporting Information. We consider three mechanically distinct model of interactions between the filaments and the obstacle, and study the fluid flows and their effect on polymerization forces in each model. For now, we neglect the coupling between the end-force and polymerization velocity, and assume all filaments are polymerizing with a fixed velocity irrespective of their end-force. This allows us to only focus on the effect of HIs on the generated flows and the drag coefficient of polymerizing filament(s).

Also, from this point on all the lengths are nondimensionalized by the length of the polymerizing filament, *L*.

Let us begin by considering a single filament polymerizing against an obstacle with a constant velocity,  $V_p$ . Since the polymerizing end of the filament is fixed at the obstacle, the polymerization forces push the filament away from the obstacle with the rate that the monomers are added that is,  $-V_p$ . This outward motion generates a flow by dragging cytoplasm from the obstacle into the fluid volume. See Figure 3a top panel. The bottom panel of Figure 3a shows the magnitude of the fluid velocity. The fluid flow is three dimensional, and the results are projected into the z-x plane for visualization. As it can be seen, because of the long-range nature of HIs, the generated flows remain strong over

distances comparable to the filament's length. Note that in all the results presented here, fluid velocity is nondimensionalized by  $V_p$ .

Next, we consider Scenario I, where the filaments within the array are all polymerizing with the same velocity against the obstacle. An example involving a similar setting is the polymerization and depolymerization of kinetochore microtubules against chromosomes in metaphase state (Joglekar, Bloom, & Salmon, 2010), and formin-mediated nucleation and rapid assembly of actin filaments (Romero et al., 2004). As shown in the top panel of Figure 3b, the flows remain strong outside of the array. This is demonstrated more clearly in the bottom panel of Figure 3b that shows the spatial variations of the fluid velocity magnitude in z - x plane, where z is the tangent direction of the filaments. The dotted white line is the contour corresponding to velocity magnitude of 0.25 of the polymerization velocity. The distances over which the velocity decays to 0.25 is roughly 0.50, compared to  $\sim$  0.3 for a single filament fluid flows.

In Scenario II, only one of the filaments is polymerizing against the obstacle, while the rest are held fixed in space. This is similar to having a polymerizing filament embedded in a network of other crosslinked filaments, such as microtubules polymerizing in a crosslinked network of actin filaments, or kinetochore microtubules (de)polymerizing against chromosomes in a crosslinked network of other microtubules within the mitotic spindle. The key mechanical feature of this condition is that the motions of the other filaments are constrained. Figure 3c shows the flow induced by the polymerizing filament (top), and the spatial variations of the fluid velocity magnitude projected into z - x plane (bottom). The transparent cylinder in the top panel marks the boundaries of the volume beyond which the flows become negligible. As it can be seen, the flow strength decays over very short distances, compared to a single filament and an array of polymerizing filaments (compare the contours). In other words, HIs between the fixed filaments significantly reduce the convective penetration of the fluid flows generated by the polymerizing filament. Thus, objects that are not within the vicinity of the polymerizing filament are hydrodynamically decoupled from it, and HIs are screened.

The filament array, therefore, can be treated as a porous volume in which the fluid permeability and the penetration length of the fluid are decreased as more filaments are included in the array. The flow inside a porous medium can be approximated using Brinkman equation (Brinkman, 1949)

$$\mu \Delta \mathbf{u} - \nabla p - \frac{\mu}{\kappa} \mathbf{u} = \mathbf{0} \& \nabla \cdot \mathbf{u} = 0, \tag{1}$$

where  $\kappa$  is the *permeability* of the porous medium. The term  $(\mu/\kappa)\mathbf{u}$  is the hydrodynamic drag force applied by the porous medium to the

fluid, because of the constrained motions of the filaments. The penetration length of the fluid into the porous medium is proportional to  $r_p = \sqrt{\kappa}$ . In Stokes regime the flows generated by a point-force decays as 1/r, where r is the separation distance from the point-force. In a Brinkman fluid, these flows decay as  $\exp(-r/r_p)/r$  (Cortez, Cummins, Leiderman, & Varela, 2010), which makes the flows negligible at  $r/r_p \gg 1$ . Brinkman equation gives good predictions of the behavior of microtubule asters within confinements, when compared against detailed simulations (Nazockdast, Rahimian, Needleman, & Shelley, 2017; Nazockdast, Rahimian, Zorin, & Shelley, 2017). Higdon and Ford (1996) give a comprehensive comparative study of the accuracy of Brinkman equation for fibrous networks over a wide range of volume fractions.

Interestingly, the array of polymerizing filaments (Scenario I) can also be modeled as a porous medium. In this case, the porous medium is moving with a net velocity of  $\mathbf{U} = -V_p\mathbf{q}$ , where  $\mathbf{q}$  is the tangent direction of the filaments. The change of variable  $\mathbf{u}' = \mathbf{u} + V_p\mathbf{q}$  makes this problem mathematically identical to having a uniform flow of  $\mathbf{u}^{\text{ext}} = V_p\mathbf{q}$  over a fixed array of filaments in Stokes flow, which is modeled by Equation (1). As the number of filaments increases the penetration length of fluid into the porous medium decreases, and the flows asymptote to those induced by a filled cylinder of radius r and length L moving with velocity  $\mathbf{U} = -V_p\mathbf{q}$ , which would produce flows similar to those shown in Figure 3b.

Table 1 lists the total force on the array of polymerizing filaments as a function of the number of filaments for r/L = 0.1 and 0.4, averaged over 30 different uniform distribution of the end-points on the surface. The forces are nondimensionalized by the drag force of a single filament with polymerization velocity,  $V_p$ . The results of the Table show for the largest values of  $N_F \infty$ , the drag forces are asymptoting to a constant number for any given r, which is the drag force of a cylinder of radius r and length L that is pushed back through the fluid along its axis with velocity magnitude  $V_p$ .

Finally, we consider scenario III, where a single polymerizing filament is placed in an array of *freely suspended* parallel filaments of the same length. Because the filaments within the array are free to move (no constraint), the net force on each filament is identically zero. Thus, the term  $(\mu/\kappa)\mathbf{u}$ , and its hydrodynamic screening effect are not present in the continuum limit. Each filament, however, has a nonzero net *force moment*. The sum of the symmetric part of these force moments determines the stress contribution of the filament phase to the *suspension*. The anti-symmetric component of the force moment tensor is identically zero, because there is no external torque acting on the filaments. In its simplest form, the stress of the filament phase can be modeled in terms of an increase in shear viscosity (Du Roure, Lindner,

**TABLE 1** The drag force on the array of polymerizing filaments as a function of the number of filaments for r/L = 0.1 and r/L = 0.4, (see Figure 2b), made dimensionless by the drag force on an individual polymerizing filament

Number of filaments (N <sub>F</sub> )	2	5	10	20	30	40
Drag force $(r/L = 0.1)$	1.73	2.45	3.07	3.49	3.75	3.95
Drag force $(r/L = 0.4)$	1.95	4.02	6.30	8.81	9.96	10.33

Note: The values converge at large enough number of filaments for each given r.

Nazockdast, & Shelley, 2019). In such conditions, the filament array can be replaced with an effective viscosity, and the induced flow would be identical to that of a single filament. The top panel of Figure 3d shows a snapshot of the generated flows of a single polymerizing filament embedded in 20 freely suspended and parallel filaments of the same length (r/L = 0.1), at early times before the filaments are displaced considerably. The flow is very similar to the flow of a single filament, which is in line with the argument that the effect of filament array is to increase the viscosity of the medium. The exact value of viscosity would have no effect on the rate of decay of the flow away from the polymerizing filament and only increases the drag force. The spatial variations of the fluid velocity magnitude near the polymerizing end, shown in the bottom panel, highlights a few differences with the single filament flows. This may arise because of flow-induced migration of heterogeneously suspended filaments. Overall, however, the flows seem fairly similar, as it is shown by their contours of  $|\mathbf{u}| = 0.25$ .

To summarize, we showed that an array of polymerizing filaments effectively behaves as a porous cylinder, with dimensions of r and L, as shown in Figure 2b, that is polymerizing with the same velocity as the individual filaments. At large, enough number of filaments, the drag force on the entire array converges to the drag of that cylinder that is being pushed away from the obstacle. These effects are direct consequences of HIs. In case of a single filament polymerizing in a fixed array of filaments, the HIs are screened, and can be neglected beyond the penetration length of fluid. If the filament is polymerizing in a bath of freely suspended filaments, HIs are *not* screened, and the main effect of the presence of the surrounding filaments is an increase in the effective viscosity of the medium, and with that an increase in the drag force on the polymerizing filament.

In the next section, we discuss the effects of HIs on the polymerization velocity, in the presence of a force-velocity relationship.

# 2.1.1 | Force-velocity relationship

Experimental and theoretical studies show that the compressive endforces reduce the polymerization velocity. This effect is described by the force-velocity relationship. As mentioned in the introduction, we do not attempt to find such a relationship here. Instead, we assume the relationship is known through experiments and theories, and take it as an input to our computations. In many asymptotic limits of the Brownian Ratchet theories (Mogilner & Oster, 1996; Peskin et al., 1993) and in many experiments (Dogterom & Yurke, 1997; Marcy et al., 2004), the force-velocity relationship can be written in the simple form of:  $V_p = V_p^0 \exp(-F/F_s)$ , where  $V_p^0$  is the polymerization velocity under no force and F<sub>s</sub> is the stall force, which is determined by microscopic parameters such as the size of the monomer, thermal energy, filament's flexural modulus and its interactions with protein complexes. We do not consider a specific form of the stall force. Instead, the results are always presented in terms of the ratios of the stall force to other forces in the problem, including the viscous and elastic forces. We do, however, require that  $F_s$  is independent of the drag or diffusion coefficients of the filaments and the obstacle. This allows us to uncouple the force-velocity relationship from HIs. Previous theories show that this assumption holds in many physiological conditions; see, for example, eq. 1 in Peskin, Odell, and Oster (1993) and eqs. E2, E4, and E10 in Mogilner and Oster (1996). In the event that this assumption does not hold, one needs to start with the original Fokker-Plank equation that describes the probability of observing the tip of the filament in space and time (see eq. 1 in Peskin, Odell, and Oster (1993) and Appendix C in Mogilner and Oster (1996)). The HIs modify the diffusion coefficient, and generate additional advective fluxes that are induced by cytoplasmic flows. Note that—even though they are not directly changing the force-velocity relationship—HIs indirectly change the polymerization force (and velocity) through balancing it with the drag force on the filament and the obstacle. This is the effect that will be explored in this study.

Again, we begin with studying the simplest case of having a rigid filament polymerizing against an obstacle from one end, while the other end is free. Because the polymerizing end is fixed at the obstacle, the polymerization forces push the filament away from the obstacle with the same velocity as the polymerization velocity, but in the opposite direction to open space for adding the newly formed filament materials. This pushing force is balanced against the hydrodynamic drag force to determine the polymerization velocity of the filament:  $-\gamma_{\parallel}V_{p}(\mathbf{q}\cdot\mathbf{n})\gamma + F = 0$ , where  $\mathbf{q}$  and  $\mathbf{n}$  are the filament's tangent vector and the obstacle's surface normal vector, and  $\gamma_{\parallel}$  is the filament's drag coefficient in its tangential direction. The term  $V_p(\mathbf{q} \cdot \mathbf{n})$  is the polymerization velocity projected in n direction. The force acting orthogonal to filament is given by the balance between the friction forces from the obstacle and the hydrodynamic drag force:  $F_{\perp} = \gamma_{\perp}(1$  $-\mathbf{q} \cdot \mathbf{n}$ ). In the absence of obstacle friction the filament will freely polymerize in tangential direction. Here, in all of our analysis, we assume that the polymerizing end of the filament is fixed (or trapped) on the obstacle, which models infinite friction with the obstacle. Also, we focus our attention to cases where filaments are parallel to the normal direction of the obstacle. The extension to the general case of the filaments that make an angle with the obstacle will be studied in future works. Combining the force-velocity relationship,  $V_p = V_p^0 \exp(-F/F_s)$ , with force balance gives

$$\gamma_{\parallel} V_n^0 \exp(-F/F_s) = F. \tag{2}$$

We scale the forces with the viscous force,  $\gamma_{\parallel}V_p^0$ , and the polymerization velocity with  $V_p^0$ . Equation (2) in dimensionless form is

$$\tilde{F} = \exp(-\tilde{F}/\tilde{F_s}), \text{ or } \tilde{V}_p = \exp(-\tilde{V}_p/\tilde{F}_s)$$
 (3)

where  $\tilde{F}_s = F_s/\left(\gamma V_p^0\right)$  is the ratio of stall force to viscous drag force, and we have dropped the subscript  $\parallel$  for convenience. Equation (3) can, then, be solved to give  $\tilde{V_p} = V_p/V_p^0$  as a function of given  $\tilde{F}_s$ . The results are shown in Figure 4 as a function of  $1/\tilde{F}_s$ . As expected,  $\tilde{V}_p$  asymptotes to 1 for  $\tilde{F}_s \gg 1$  and approaches zero for  $\tilde{F}_s \ll 1$ .

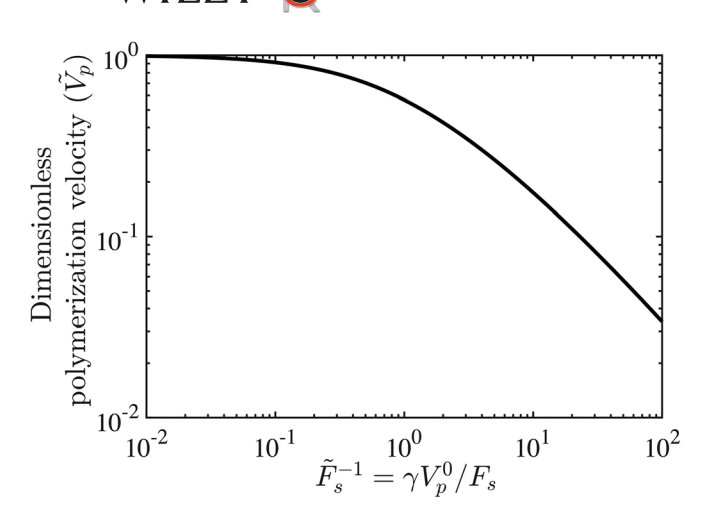


**FIGURE 4** The dimensionless polymerization velocity (scaled with the polymerization velocity under no compressive force) as a function of the ratio of viscous to stall force,  $\tilde{F}_s^{-1} = \left(\gamma V_p^0\right)/F_s$ , for a rigid filament. The results are obtained by balancing the polymerization force against the hydrodynamic drag force:  $\tilde{V}_p = \exp\left(-\tilde{V}_p/\tilde{F}_s\right)$ . The line is the solution to this equation

We now consider the effect of HIs between the array of filaments on the polymerization velocity of the filament. We specifically ask how does the presence of other filaments change the end-force on the polymerizing filaments? Once the end-force is known, the polymerization velocity can be computed using force-velocity relationship. Another useful definition to consider in this context is the effective drag coefficient,  $\gamma_{\rm eff}$ , defined as the ratio the end-force on the filament to the velocity by which the filament is pushed back toward the fluid:  $\gamma_{\rm eff} = F_{\rm end}/V_p^0$ . Once  $\gamma_{\rm eff}$  is computed from simulations,  $F_s$  can be evaluated using the computed value for effective drag coefficient:  $\tilde{F}_s = F_s/\left(\gamma_{\rm eff}V_p^0\right)$ . Having calculated  $\tilde{F}_s$ , the polymerization velocity can be calculated from the curve in Figure 4.

In the previous section, we showed that for an array of polymerizing filaments the net force on the entire array converges to a constant (see Table 1). As a result, the average force per filament (as well as  $\gamma_{\rm eff}$ ) is continuously reduced with the number of filaments, and at large  $N_F$  it reduces as  $1/N_F$ . This is demonstrated in Figure 5a, that shows the force per filament versus  $N_F$  for 30 different distribution of end-points on the obstacle's surface of dimensionless radii r=0.1,0.4, and 1. The ensemble average values are plotted with a thicker line. This reduction in the end-force (and  $\gamma_{\rm eff}$ ) significantly increases the polymerization velocity at large  $N_F$ . This is illustrated in Figure 5b for different ratios of stall force to viscous force,  $\tilde{F}_s$ , and r=0.1. Same qualitative behavior is observed in other values of r.

For example, consider a microtubule of length  $L=5~\mu m$ , and  $F_s=4pN$  (Dogterom & Yurke, 1997), is polymerizing with  $V_p^0=0.7\mu m/s$  (Srayko, Kaya, Stamford, & Hyman, 2005) against an obstacle of radius  $r=1~\mu m$ , and immersed in a fluid of viscosity  $\mu=1~{\rm Pa\cdot s}$ , while the other end is inactive and free. The drag coefficient of a microtubule of radius 12 nm along its axis is  $\gamma=(4\pi\mu L)/{\rm ln}$ 

 $(\epsilon^2 e^{-1}) = 5.84 \text{pN} \cdot \text{s/\mu m}$ , where  $\epsilon \ll 1$  is the ratio of the filament's radius to its length,  $\mu$  is the effective viscosity of the medium, and  $k_b$ is the Boltzmann coefficient. This makes the ratio of viscous to stall force  $\sim \tilde{F}_{c}^{-1} = 1.0$ . We can evaluate the dimensionless polymerization velocity by interpolating the results of Figure 4, which gives  $\tilde{V}_n = 0.56$ . The end-force can then be computed using force-velocity relationship:  $F = -F_s \ln(\tilde{V}_p) = 2.3 \text{pN}$ . Now consider an array of 20 microtubules that are polymerizing against the same obstacle. We can use the results of Table 1 to evaluate the effective drag coefficient of each filament in the array with r/L = 0.2 as  $\gamma_{\rm eff} = 3.49 \times \gamma/20 = 1.02 \, \rm pN \cdot s/\mu m$ . Using this value we can compute the ratio of viscous to stall force:  $\tilde{F}_s^{-1} = 0.18$ . Then, we use Figure 4 to compute  $\tilde{V}_p = 0.86$ , and F = 0.6pN for each microtubule and  $F^{T} = 12.1$ pN for the entire array. This force is roughly five times larger than a single microtubules (compared to 20 times if they were hydrodynamically uncoupled). Doubling the number of microtubules in the array to  $N_E$  = 40 only changes the total force to 15.1pN.

An important point to note is that if the filaments within the array were depolymerizing instead, their effect on the polymerizing filament would have been reversed: The end-force on the polymerizing filament (as well as  $\gamma_{\rm eff}$ ) would have increased, resulting in a reduction in  $V_p$ , compared to a single filament. This occurs because the depolymerizing filaments would generate flows that are in the opposite direction of those generated by polymerizing filament, thereby pulling the filament toward (instead of away from) the obstacle and increasing the needed force to push the filament away from the obstacle. Conditions become more complicated when filaments are concurrently polymerizing and depolymerizing against boundaries. Detailed simulations are needed to study the effect of HIs in such conditions.

We now consider Scenario II. Figure 5c shows the end-force on a single filament polymerizing against an obstacle in array of fixed filaments as function of  $N_F$  for 60 different uniform distribution of end-points on the obstacle surface of radius r=0.1. The presence of fixed filaments reduces the penetration length of the fluid. This is analogous to having an outer boundary with roughly the dimensions of the penetration length around the filament (Nazockdast, Rahimian, Needleman, & Shelley, 2017; Nazockdast, Rahimian, Zorin, & Shelley, 2017). This confinement effect causes the drag force (and  $\gamma_{\rm eff}$ ) to increase with  $N_F$ , which then leads to a decrease in the polymerization velocity as shown in Figure 5d. However, the effects are not as strong as those observed for polymerizing filaments, mainly because the filament is slender and the confinement effects from fixed filaments array can only weakly change the drag force.

# 2.2 | Flexible polymerizing filaments

Next, we study the effect of filament's flexibility on the generated flows, and the polymerization forces and velocities. We focus on the limit where viscous forces are significantly larger than the thermal forces, so that the filament's dynamics is dominated by viscous forces. The ratio of advection velocity of the filament, that is induced by polymerization

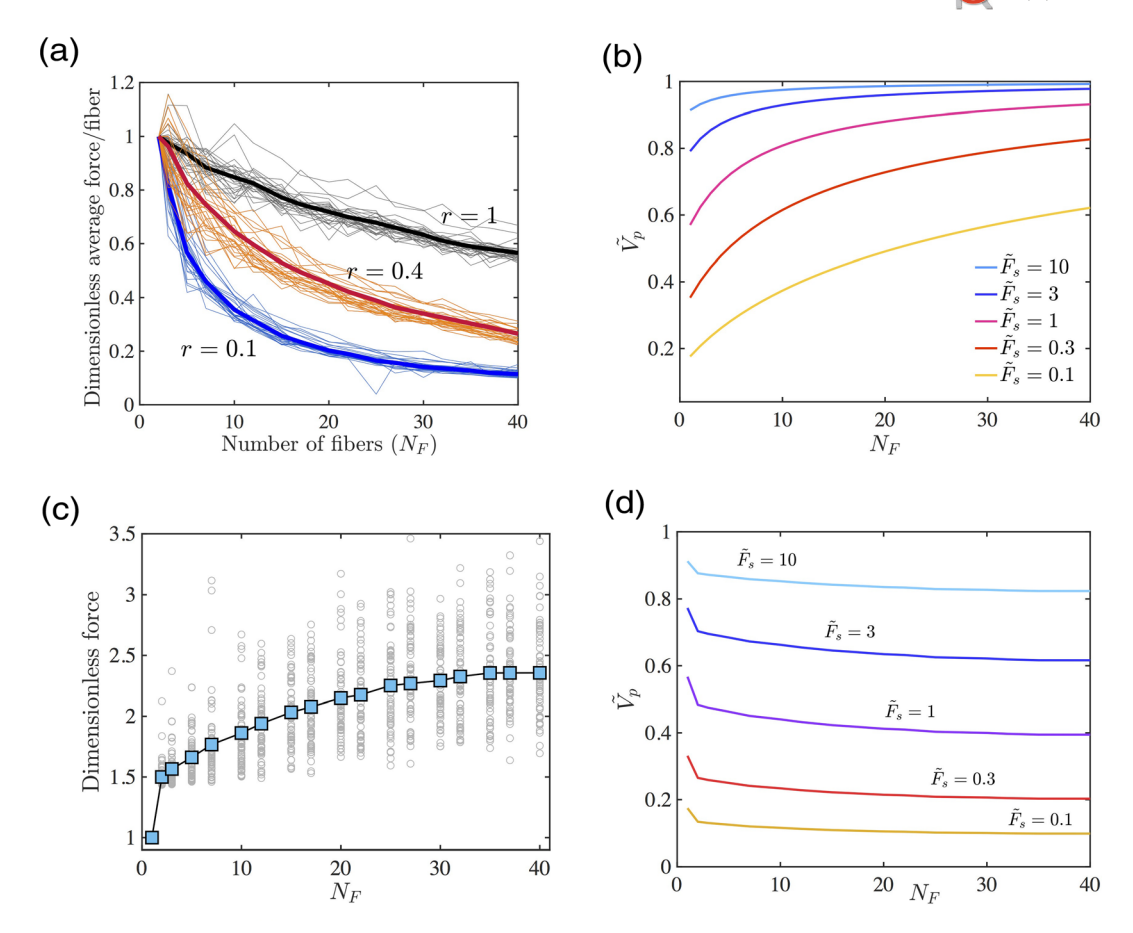


**FIGURE 5** (a) The average force per filament as a function of the number of polymerizing filaments ( $N_F$ ), made dimensionless by the drag force on a single filament. The filaments are uniformly distributed over surfaces of dimensionless radius r = 0.1, 0.4, and 1. The thicker solid lines are the forces for each r, averaged over 30 different uniform distribution of attachment points; the result of each distribution is shown with thinner (lighter) lines. (b) Average polymerization velocity of an array of polymerizing filaments against the obstacle versus  $N_F$ , for an array with r = 0.1 and for different values of  $\tilde{F}_s = F_s/V_p^0 \gamma$ . (c) The dimensionless end-force on a polymerizing filament, embedded in an array of fixed filaments of the same length and r = 0.1; the filled square symbols are the forces, averaged over 60 different uniform distributions of attachment points over the surface (open circles). (d) Filament's polymerization velocity at different values of  $\tilde{F}_s$  as a function of the number of fixed filaments [Color figure can be viewed at wileyonlinelibrary.com]

forces, to thermal diffusion velocity is given by Péclet number defined as  $Pe = V_p \gamma L/k_b T$ . The assumption of  $Pe \gg 1$  is expected to hold in many cellular settings. For example, for a microtubule of length  $2\,\mu m$ immersed in C. elegans embryo of cytoplasmic viscosity of  $\mu = 1$  Pa · s (Daniels, Masi, & Wirtz, 2006), the Péclet number is Pe = 408. When  $Pe \gg 1$ , we can ignore the filament's net displacement due to thermal diffusion, in comparison to those induced by viscous forces. To compare the deformations induced by viscous and thermal forces both forces should be evaluated in the length-scale of the persistence length of filament, l<sub>p</sub>. This modifies the Péclet number  $Pe = 4\pi\mu V_p I_p^2 / (k_b T \ln(\epsilon^{-2} e^{-1}))$ . Since  $I_p / L \gg 1$  for microtubules and  $I_p/L > 1$  for most actin-based processes, we expect the thermal undulations to be negligible in comparison to buckling and bending deformations induced by viscous forces, if the initial assumption of  $V_p \gamma L/k_p T \gg 1$  holds. We should note that we are only discussing the filament's deformations beyond the buckling instability. Below the buckling threshold and in the special case of a filament orthogonal to the obstacle, the viscous forces only cause a net motion of the filament and the deformations are entirely induced by thermal undulations. Note also that if the filament is not orthogonal to the obstacle, it will bend under viscous forces well below the buckling threshold.

The shape of a flexible filament is time-dependent. The lengths of polymerizing filaments are monotonically increasing with time. Elastic forces scale as  $F_E \sim E/L^2$  and the viscous forces scale as  $F_V = V_p^0 \gamma$ , which makes their ratio  $\tilde{\eta} = F_V/F_E = 4\pi\mu V_p^0 L^3/(\ln(\varepsilon^{-2}e^{-1})E)$ . We can see that  $\tilde{\eta}$  monotonically increases as  $L^3$  with time and, thus, the filament shape and dynamics will not reach to a mechanical steady-state. The mechanical problem in this form cannot be systematically analyzed in terms of the ratios of viscous, elastic and stall forces. To circumvent this issue we assume that the free end of the flexible filaments are shrinking with the same rate as their other end is polymerizing, so that the length of the filament remains unchanged with time. Note that the shrinking process of the free end does not apply any force to the fluid, and has no effect on the mechanics other than fixing the length of the filament. In

this treatment of the problem the ratio of the mentioned forces are fixed in time, and mechanical steady-state can be achieved.

Let us consider a straight filament and introduce small deformations along its length, say from thermal fluctuations. These deformations can either relax (disappear) over time, or-if the compressive forces are strong enough-they can grow with time and lead to buckling instability. We have analyzed the transition to buckling instability by performing linear stability analysis of the dynamic equations that describe the filament's shape, which will be presented in later publications. Our stability analysis and simulation results show that the transition occurs at roughly  $\tilde{\eta}_c$  = 202. As an example, Figure 6 shows different simulation snapshots of a buckled filament polymerizing against an infinite wall with a constant velocity at  $\tilde{\eta}$  = 380, as well as the generated cytoplasmic flows. Clamped boundary condition was used in these simulations, that is, the angle of attachment was fixed throughout the simulation. A video (anchor.mp4) of this simulation is provided in Supporting Information. As expect, the generated flows are qualitatively different from those observed for straight filaments (see Figure 3a), and change direction with the beating of the filament. Changing the boundary condition to hinged results in qualitatively different shape of the buckled filament, and the transition occurs at different ratios of viscous to elastic forces. A video (hinged.mp4) depicting the simulation results for hinged boundary condition at  $\tilde{\eta}$  = 435 is provided in Supporting Information.

# 2.2.1 | The effects of HIs on buckling transition

We now discuss how HIs change the buckling transition in Scenarios I, II, and III. Buckling transition occurs when the ratio of tangential force

on the polymerizing end to the elastic forces exceeds a critical value:  $F_{\rm end}L^2/E=\tilde{\eta}>\tilde{\eta}_c\approx 202$ , where  $F_{\rm end}=\gamma V_p^0$  is the force on the polymerizing end. We showed in Section 2.1 that for an array of straight polymerizing filaments, the end-force continuously decreases with increasing the number of filaments within the array. Because of this reduction in end-forces, the buckling transition occurs at larger values of  $\tilde{\eta}$ , when compared to a single filament. For example, in an array with r=0.1 and  $N_F=20$  the end-forces reduce to 0.20 of the value for a single filament; see Figure 5b. Because the flexible filaments remains straight before the buckling transition, their compressive forces are identical to those of the rigid filaments. Thus, the buckling instability in this array is expected to occur at  $\tilde{\eta}_c=202\times 5=1,010$ . This can be confirmed by formal linear stability analysis and detailed simulations (to be published elsewhere).

For a single filament polymerizing in an array of fixed filaments, the end-force is increased with  $N_F$  due to an increase in the effective drag coefficient; Thus, the buckling transition occurs, accordingly, at lower values of  $\tilde{\eta}$ . Finally, in the case of a filament polymerizing in an array of freely suspended filaments, the presence of filaments increases the end-force by increasing the effective viscosity of the medium and the transition to buckling is expected to occur at lower  $\tilde{\eta}$ . We are in the process of performing these simulations for a large number of freely suspended filaments.

# 2.2.2 | The effect of buckling on the polymerization velocity

As the filament undergoes buckling instability, its end-force is reduced. As a consequence, the polymerization velocity of a flexible

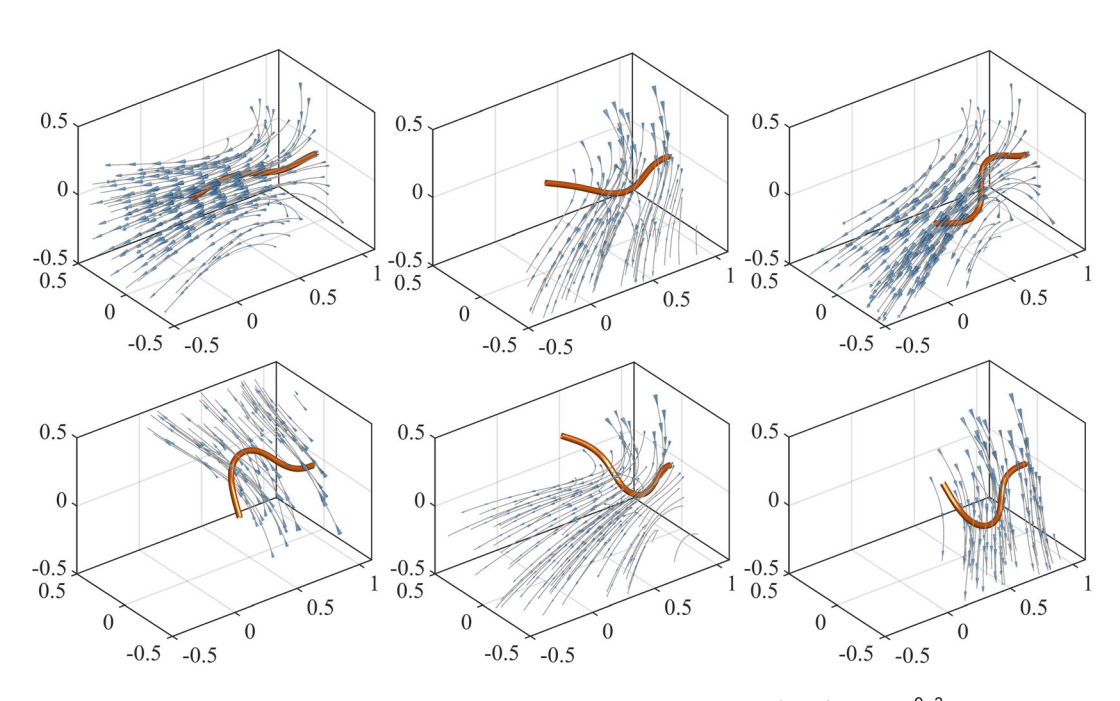


**FIGURE 6** Snapshots of the simulation of a single filament polymerizing against an obstacle (z = 1) at  $\tilde{\eta} = \gamma V_p^0 L^2 / E = 383$ , and flows induced by it. The polymerization induces a buckling instability, which results in qualitatively different flows compared to the flow of a rigid polymerizing filament; see Figure 3a for the generated flow of a rigid filament [Color figure can be viewed at wileyonlinelibrary.com]

filament is expected to increase in comparison with a rigid filament under identical physical conditions and for a given force-velocity relationship. Figure 7a shows the variations of the polymerization velocity (left-axis) and the end-force (right-axis) as a function of time at  $\tilde{\eta}=1,550$  and  $F_s/F_b=0.80$ , where  $F_b=202E/L^2$  is the critical buckling instability force. The large rate of decay (increase) of the end-force (polymerization velocity) at early times is associated with the filament's buckling transition, while the small amplitude oscillations of the end-force and  $\tilde{V}_p$  at long times is due to the beating of the buckled filament. The end-force and polymerization velocity at very early times (before the sharp decay) correspond to those values for a rigid filament.

Figure 7b shows the variations of dimensionless polymerization velocity,  $\tilde{V}_p$ , with the ratio of viscous to stall force,  $\tilde{F}_s^{-1}$ , for different ratios of  $F_s/F_b$ . Note that in defining  $\tilde{F}_s = F_s/\gamma V_p^0$  we have used the polymerization velocity in the absence of the end-force,  $V_p^0$ . As it can be seen, at small values of  $\tilde{F}_s^{-1}$  and small ratios of  $F_s/F_b$  the forcevelocity curves become independent of  $F_s/F_b$ , and asymptote to the curve of a rigid filament. The deviation from the rigid filament curve coincides with the transition to buckling. To show this consider the product  $\tilde{V}_p \tilde{F}_s^{-1} F_s/F_b$ , which can be simplified as

$$\tilde{V}_{p}\tilde{F}_{s}^{-1}\frac{F_{s}}{F_{b}} = \frac{V_{p}\gamma V_{p}^{0}F_{s}}{V_{p}^{0}F_{s}}\frac{F_{b}}{F_{b}} = \frac{\gamma V_{p}}{F_{b}}.$$
(4)

Noting that if  $V_{\rho}$  is the polymerization velocity under compressive force, the product is simply the ratio of the end-force to the critical buckling instability force. As expected, the deviation from the rigid filament curve and filament buckling occur when this ratio is larger than one:  $\tilde{V}_{\rho}\tilde{F}_{s}^{-1}\frac{F_{s}}{F_{s}} > 1$ .

The results of Figure 7b can be extended to compute the polymerization velocity in Scenarios I, II, and III, by replacing  $\gamma$  with the computed values of  $\gamma_{\rm eff}$ , when evaluating the ratio of stall to viscous forces:  $\tilde{F}_s = F_s / \left(\gamma_{\rm eff} V_p^0\right)$ . Other quantities, including  $F_b$ , are unchanged, as they are not dependent on HIs.

As an example, consider a microtubule of length  $L=5~\mu m$ , flexural modulus of  $10 p N \mu m^2$  (Howard, 2001) and  $F_s=32 p N$ , is polymerizing with  $V_p^0=0.7 \mu m/s$  against a chromosome within a spindle with effective viscosity of  $\mu=2.4\times 10^2 Pa\cdot s$  (Shimamoto, Maeda, Ishiwata, Libchaber, & Kapoor, 2011). The drag coefficient of the microtubule is  $\gamma=(4\pi\mu L)/ln(\epsilon^2 e^{-1})=1402 p N\cdot s/\mu m$ , and the ratio of viscous to stall force is  $\tilde{F}_s^{-1}=30.67$ . Having  $F_b=202 E/L^2=80 p N$ , we can compute the ratio of stall to buckling instability force:  $F_s/F_b\approx 0.4$ . We evaluate the polymerization velocity by interpolating the results of Figure 7b for  $F_s/F_b=0.4$  and  $\tilde{F}_s^{-1}=30.67$ . Interpolation gives  $\tilde{V}_p=0.23$  (or  $V_p=0.16~\mu m/s$ ), and also shows that the microtubule is in the buckled regime. The end-force can, then, be computed using force-velocity relationship:  $F=-F_s ln\left(\tilde{V}_p\right)=47 p N$ . Note that because the end-force is significantly reduced after buckling, the computed value is less than the buckling instability force.

Now consider the case of an array of 20 microtubules of the same length, polymerizing over a chromosome modeled here as a disk with radius of 1  $\mu$ m (r/L = 0.1). We can use Table 1 to approximate the effective drag coefficient of each microtubule as  $\gamma_{\rm eff}$  = 3.49 $\gamma$ /20 = 244.5pN ·  $s/\mu$ m, and compute  $\tilde{F}_s^{-1}$  = 7.6, which is slightly below the buckling transition point at  $F_s/F_b$  = 0.4. Thus, in this scenario the microtubules will be remain straight. We then interpolate the results of Figure 7b, to compute  $\tilde{V}_p$  = 0.35. The force-velocity relationship is

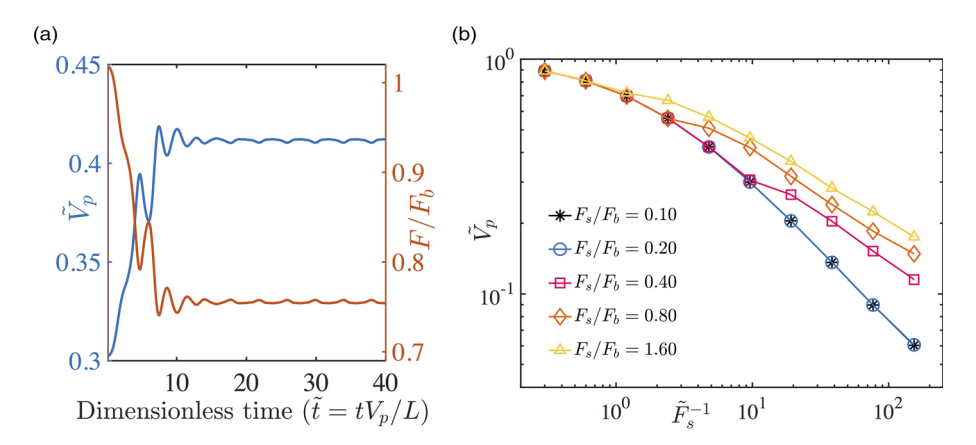


**FIGURE 7** (a) Variations of the polymerization velocity (left-axis) and the end-force (right-axis) plotted as a function of dimensionless time,  $\tilde{t} = tV_p^0/L$ , at  $\tilde{\eta} = 1,550$  and  $F_s/F_b = 0.8$ , where  $F_b = 202E/L^2$  is the critical buckling instability force. The sharp variations of the end-force and p at early times is associated with the buckling transition. Small oscillations of  $\tilde{V}_p$  and the end-force at long times is due to the beating motion of the buckled filament. (b) Filament's polymerization velocity as a function of the ratio of viscous to stall force,  $\tilde{F}_s^{-1} = \gamma V_p^0/F_s$ , plotted at different ratios of stall force to critical buckling instability force,  $F_s/F_b$ . Note that the product  $V_p\tilde{F}_s^{-1}(F_s/F_b)$  is simply  $(\gamma V_p)/F_b$ . Thus when  $\gamma V_p/F_b < 1$ , the filament remains straight and the results asymptote to those of a rigid filament. When  $\gamma V_p/F_b > 1$ , the filament buckles, which causes a decrease in the end-force and an increase in the polymerization velocity [Color figure can be viewed at wileyonlinelibrary.com]

then used to compute the end-force per microtubule as  $F \approx 34 \text{pN}$ , making the total force on the chromosome equal to  $F^T = 680 \text{pN}$ .

Note that such approximations remain accurate as long as the flow generated by the surrounding filaments on each filament is uniform along the filament's length that is, the flow gradients along the filaments are small. Strong flow gradients can result in a complex range of behaviors, such as the buckling of filaments in shear and extensional flows (Du Roure et al., 2019; Guglielmini, Kushwaha, Shaqfeh, & Stone, 2012; Tornberg & Shelley, 2004). For a more rigorous treatment of the problem see Stein and Shelley (2019), where a coarse-grained model of arrays of flexible filaments is developed. In the examples studied here the filaments are uniformly distributed, parallel and of equal length and polymerization velocities. Because of these simplifications, the generated flows by the surrounding filaments are roughly uniform along its length, which can be seen in Figure 3. Relaxing any of these assumptions may lead to more complex flows. Consider, for example, a polymerizing filament surrounded by an array of filaments with two populations of filaments that are concurrently polymerizing and depolymerizing against the obstacle with equal likelihood (see the top panel of Figure 8). The bottom panel of Figure 8 shows the flows generated by such an array, as well as the resulting shape of the polymerizing filament within that array.

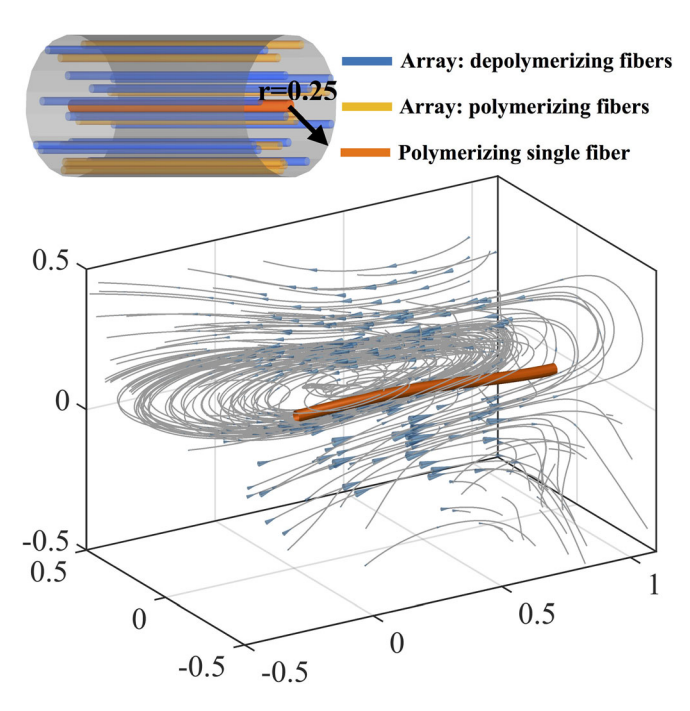


**FIGURE 8** Top panel: Schematic representation of a polymerizing filament (shown as the thicker filament in the center of the cylindrical array), embedded in an array of filaments that are polymerizing (yellow) and depolymerizing (blue) simultaneously and with equal probability. Bottom panel: The embedded polymerizing filament and the flows induced by the array of (de)polymerizing filaments. The simulations were performed at  $\tilde{\eta}=100$ , which is below the critical buckling instability  $\tilde{\eta_c}=202$ . Yet, the flows induced by the array cause the polymerizing filament to slightly buckle [Color figure can be viewed at wileyonlinelibrary.com]

Because of equal likelihood of polymerization and depolymerization, once averaged over time, the array does not apply a net force to the polymerizing filament. Nevertheless, as the figure shows, strong flow gradients can be generated along the filament's length. Because of these flow gradients the filament is slightly buckled at  $\tilde{\eta}=100$ , which is below the buckling instability limit of a single filament ( $\tilde{\eta_c}=202$ ). Careful computational studies are needed to study the effect of variations of length, polymerization velocities, and the angles between the filaments and the obstacles on HIs, and the resulting polymerization forces and velocities.

# 2.2.3 | Bundling of buckled filaments by HIs

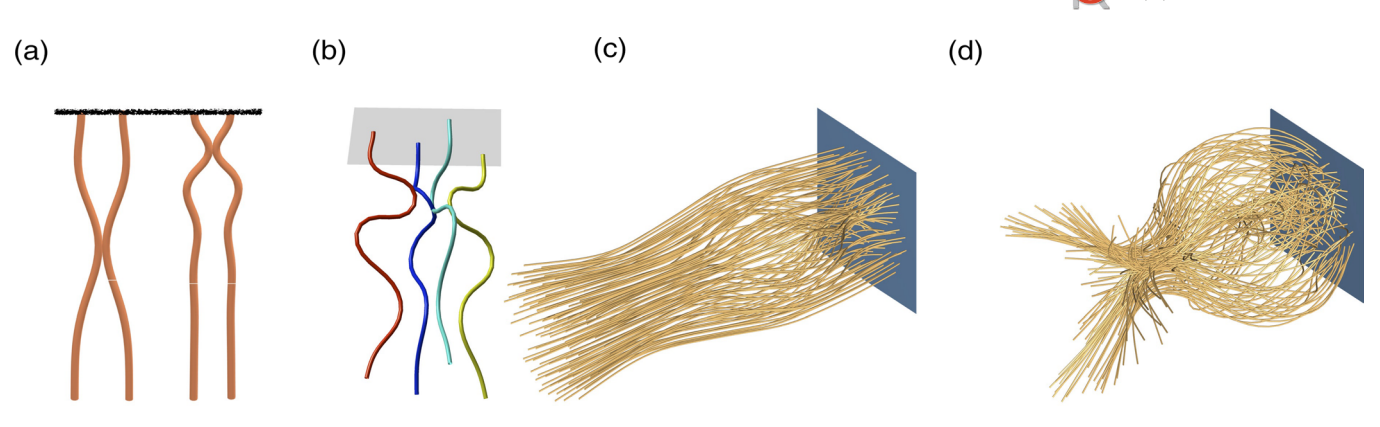
Next, we explore the effect of HIs on the dynamics of an array of buckled filaments. Figure 9a shows snapshots of two simulations of a pair of filaments polymerizing against an obstacle. The pushing forces are strong enough to induce buckling instability in both filaments. The simulations were done in 3D and clamped boundary condition was used for the polymerizing ends. In the snapshot to left, the pushing forces are slightly above the buckling instability of the pair, and in the snapshot to the right, the forces are significantly larger. As a result, higher frequency (shorter wavelength) modes of buckling are produced in the filament with larger end-forces. In both simulations HIs cause the filaments to bundle at points where their buckling deformations are maximized. To ensure that the observed behavior is not a numerical artifact, we have run the simulations for several different discretization in time and space; we observe numerical convergence in all cases. We have also varied the initial spacing between the filaments, and have changed the boundary condition from clamped to hinged. The same quantitative behavior was observed in all these perturbations.

Figure 9b shows a snapshot of the simulation results for four filaments at values of  $\tilde{\eta}$  significantly above the buckling instability of the filaments. The same bundling of filaments is observed: The dark blue filament is in touch with both the red and light blue filaments, and the yellow filament is approaching the point of contact between the dark blue and light blue filaments. Similar to pair of filaments, the bundling occurs at locations where the buckling amplitudes are maximized.

Interestingly, the same behavior is observed in larger assemblies of polymerizing filaments. Figure 9c,d shows snapshots of simulation of 150 polymerizing filaments against a boundary in early and later stages of buckling. Hinged boundary conditions were used in these simulations. Again, we see the bundling of many filaments, at locations that their buckling amplitudes are the largest. These results suggest that the bundling occurs irrespective of the details of boundary conditions and the number of filaments. Further studies are needed to understand the underlying physics of this bundling behavior.

# 3 | CONCLUDING REMARKS

Polymerization of cytoskeletal filaments against boundaries is known to produce forces and motion in cellular materials, including cell



**FIGURE 9** (a) Two simulation snapshots of a pair of filaments that are polymerizing against an obstacle. In the left snapshot, the viscous forces are slightly above the buckling instability of the two-filaments. In the right snapshot, the viscous forces are significantly larger, resulting in higher frequency (shorter wavelength) modes of buckling instability. In both scenarios HIs act as pair attractive forces between locations where buckling is maximized. The tangent vector at the polymerizing end were kept constant throughout the simulations (clamped). (b) Simulation snapshot of four strongly buckled filaments that are polymerizing against an obstacle (gray surface). The same bundling of filaments is observed. (c,d). Snapshots of simulations of 150 polymerizing filaments in the early (c) and later (d) stages after the onset of buckling instability. Hinged boundary condition was used in these simulations. In both instances, HIs cause several filaments to *bundle* where their buckling is maximized, similar to what is observed for a filament pair and four filaments (Figures 9a,b) [Color figure can be viewed at wileyonlinelibrary.com]

motility driven by actin polymerization and chromosome motions induced by kinetochore microtubules assembly and disassembly. These motions of the cytoskeletal filaments induce large-scale and long-range cytoplasmic flows and HIs between the filaments and other cellular objects. Previous theoretical and computational studies of polymerization forces in the cytoskeleton largely ignore HIs. In this study, we used detailed dynamic simulations that explicitly account for HIs to demonstrate several important consequences of HIs on filaments' polymerization forces and velocities against obstacles.

To demonstrate the fundamental differences between the HIs in various mechanical conditions, we chose a simple model system composed of a filament polymerizing against an immobile obstacle, and surrounded by an array of parallel filaments of the same length with ends that are uniformly distributed over a disk-like domain on the obstacle (see Figure 2a). We assumed three distinct mechanical conditions for the filaments within the array: (a) The filaments were polymerizing with the same velocity; (b) they were held fixed in space; and (c) they were freely suspended. Through simulations, we showed that each of these conditions produces its unique HIs, and results in significantly different polymerization forces and velocities. We, then, studied the effect of buckling of flexible filaments on the polymerization forces and velocities, and discussed the effect of HIs in the three mentioned conditions on the onset of buckling transition. Finally, we showed that HIs can lead to the bundling of polymerizing filaments, in points where their buckling amplitudes are maximized; see Figure 9.

The model system studied here is, nevertheless, much simpler than the cytoskeletal structures in physiological conditions. For example, the length of microtubules and actin filaments within an assembly can greatly vary, the filaments are not always parallel and do not necessarily polymerize orthogonal to the boundaries, and the filaments may be simultaneously polymerizing and depolymerizing. Most importantly, we have ignored the active forces from motor-proteins and

crosslinkers, which are key to the structure and mechanics of the cytoskeleton. The effect of cytoplasmic flows and long-range fluidstructure interactions in the presence of these forces and geometrical variations remain largely unknown, even when the microscopic interactions of motors and filaments are well-understood. Many more computational studies are needed to explore these effects, which will certainly lead to a host of interesting and complex phenomena involving the interactions of fluid flows with cytoskeletal structures. These findings are key to developing microscopic coarse-grained theories for the fluid dynamics of active cellular organizations (Mogilner & Manhart, 2018; Shelley, 2016). Recent advancements in microscopy have enabled us to visualize cytoskeletal components and measure the involved dynamical variables with unprecedented resolutions (Chen et al., 2014; Redemann et al., 2017). Full integration of this microstructural data with dynamic simulations, that are equally detailed in their structural and dynamical descriptions, will enable developing models that can predict the behavior of the cytoskeleton from individual filaments to the collective behavior of the assembly.

# **ACKNOWLEDGMENTS**

I would like to thank M. Shelley for the stimulating discussions.

### **DATA AVAILABILITY STATEMENT**

The data that support the findings of this study are openly available in Cytoskeleton2019Repository.

# **REFERENCES**

Atzberger, P. J., Kramer, P. R., & Peskin, C. S. (2007). A stochastic immersed boundary method for fluid-structure dynamics at

- microscopic length scales. *Journal of Computational Physics*, 224(2), 1255-1292.
- Bausch, A., & Kroy, K. (2006). A bottom-up approach to cell mechanics. *Nature Physics*, 2(4), 231.
- Bottino, D., Mogilner, A., Roberts, T., Stewart, M., & Oster, G. (2002). How nematode sperm crawl. *Journal of Cell Science*, 115(2), 367–384.
- Bottino, D. C., & Fauci, L. J. (1998). A computational model of ameboid deformation and locomotion. *European Biophysics Journal*, 27(5), 532–539.
- Bray, D. (2000). Cell movements: from molecules to motility. New York: Garland Science.
- Brinkman, H. C. (1949). A calculation of the viscous force exerted by a flowing fluid on a dense swarm of particles. *Applied Scientific Research*, 1(1), 27–34.
- Brugués, J., & Needleman, D. (2014). Physical basis of spindle self-organization. *Proceedings of the National Academy of Sciences*, 111(52), 18496–18500.
- Cameron, L. A., Footer, M. J., Van Oudenaarden, A., & Theriot, J. A. (1999). Motility of acta protein-coated microspheres driven by Actin polymerization. Proceedings of the National Academy of Sciences, 96(9), 4908–4913.
- Chen, B.-C., Legant, W. R., Wang, K., Shao, L., Milkie, D. E., Davidson, M. W., ... English, B. P. (2014). Lattice light-sheet microscopy: Imaging molecules to embryos at high spatiotemporal resolution. *Science*, 346(6208), 1257998.
- Cogan, N., & Guy, R. D. (2010). Multiphase flow models of biogels from crawling cells to bacterial biofilms. *HFSP Journal*, 4(1), 11–25.
- Cortez, R., Cummins, B., Leiderman, K., & Varela, D. (2010). Computation of three-dimensional brinkman flows using regularized methods. *Journal of Computational Physics*, 229(20), 7609–7624.
- Daniels, B. R., Masi, B. C., & Wirtz, D. (2006). Probing single-cell micromechanics in vivo: The microrheology of *C. elegans* developing embryos. *Biophysical Journal*, 90(12), 4712–4719. https://doi.org/10.1529/biophysi.105.080606
- Dembo, M., & Harlow, F. (1986). Cell motion, contractile networks, and the physics of interpenetrating reactive flow. *Biophysical Journal*, 50(1), 109–121
- Dickinson, R. B., Caro, L., & Purich, D. L. (2004). Force generation by cytoskeletal filament end-tracking proteins. *Biophysical Journal*, 87(4), 2838–2854.
- Dogterom, M., & Yurke, B. (1997). Measurement of the force-velocity relation for growing microtubules. *Science*, 278(5339), 856–860. https://doi.org/10.1126/science.278.5339.856
- Du Roure, O., Lindner, A., Nazockdast, E. N., & Shelley, M. J. (2019). Dynamics of flexible fibers in viscous flows and fluids. *Annual Review of Fluid Mechanics*, 51, 539–572.
- Fabry, B., Maksym, G. N., Butler, J. P., Glogauer, M., Navajas, D., & Fredberg, J. J. (2001). Scaling the microrheology of living cells. *Physical Review Letters*, 87(14), 1–4. https://doi.org/10.1103/PhysRevLett.87. 148102
- Footer, M. J., Kerssemakers, J. W., Theriot, J. A., & Dogterom, M. (2007). Direct measurement of force generation by actin filament polymerization using an optical trap. *Proceedings of the National Academy of Sciences*, 104(7), 2181–2186.
- Garzon-Coral, C., Fantana, H. A., & Howard, J. (2016). A force-generating machinery maintains the spindle at the cell center during mitosis. *Science*, 352(6289), 1124–1127.
- Guglielmini, L., Kushwaha, A., Shaqfeh, E. S., & Stone, H. A. (2012). Buckling transitions of an elastic filament in a viscous stagnation point flow. Physics of Fluids, 24(12), 123601.
- Higdon, J., & Ford, G. (1996). Permeability of three-dimensional models of fibrous porous media. *Journal of Fluid Mechanics*, 308, 341–361.
- Holz, D., & Vavylonis, D. (2018). Building a dendritic Actin filament network branch by branch: Models of filament orientation pattern and

- force generation in lamellipodia. *Biophysical Reviews*, 10(6), 1577–1585.
- Howard, J. (2001). Mechanics of motor proteins and the cytoskeleton (1st ed.). Sunderland, Massachusetts: Sinauer Associates, Inc.
- Joglekar, A. P., Bloom, K. S., & Salmon, E. (2010). Mechanisms of force generation by end-on kinetochore-microtubule attachments. Current Opinion in Cell Biology, 22(1), 57–67.
- Johnson, R. E. (1980). An improved slender-body theory for stokes flow. Journal of Fluid Mechanics, 99(02), 411. https://doi.org/10.1017/ S0022112080000687
- Joung, C., Phan-Thien, N., & Fan, X. (2001). Direct simulation of flexible fibers. *Journal of Non-Newtonian Fluid Mechanics*, *99*(1), 1–36.
- Keller, J., & Rubinow, S. (1976). Slender-body theory for slow viscous flow. Journal of Fluid Mechanics, 75, 705-714 Retrieved from http://journals.cambridge.org/abstract\_S0022112076000475
- Kovar, D. R., & Pollard, T. D. (2004). Insertional assembly of Actin filament barbed ends in association with formins produces piconewton forces. Proceedings of the National Academy of Sciences, 101(41), 14725–14730.
- Kruse, K., Joanny, J.-F., Jülicher, F., Prost, J., & Sekimoto, K. (2005). Generic theory of active polar gels: A paradigm for cytoskeletal dynamics. The European Physical Journal E, 16(1), 5–16.
- Lim, S., & Peskin, C. S. (2012). Fluid-mechanical interaction of flexible bacterial flagella by the immersed boundary method. *Physical Review E*, 85 (3), 036307.
- Marcy, Y., Prost, J., Carlier, M.-F., & Sykes, C. (2004). Forces generated during Actin-based propulsion: A direct measurement by micromanipulation. Proceedings of the National Academy of Sciences, 101(16), 5992-5997
- Moeendarbary, E., Valon, L., Fritzsche, M., Harris, A. R., & Dale, A. (2013). The cytoplasm of living cells behaves as a poroelastic material. *Nature Materials*, 12(3), 253–261. https://doi.org/10.1038/nmat3517.The
- Mogilner, A. (2006). On the edge: Modeling protrusion. *Current Opinion in Cell Biology*, 18(1), 32–39.
- Mogilner, A., & Manhart, A. (2018). Intracellular fluid mechanics: Coupling cytoplasmic flow with active cytoskeletal gel. *Annual Review of Fluid Mechanics*, 50, 347–370.
- Mogilner, A., & Oster, G. (1996). Cell motility driven by actin polymerization. *Biophysical Journal*, 71(6), 3030–3045.
- Nazockdast, E., Rahimian, A., Needleman, D., & Shelley, M. (2017). Cytoplasmic flows as signatures for the mechanics of mitotic positioning. *Molecular Biology of the Cell*, 28(23), 3261–3270.
- Nazockdast, E., Rahimian, A., Zorin, D., & Shelley, M. J. (2017). A fast platform for simulating semi-flexible fiber suspensions applied to cell mechanics. *Journal of Computational Physics*, 329, 173–209.
- Nedelec, F., & Foethke, D. (2007). Collective Langevin dynamics of flexible cytoskeletal fibers. New Journal of Physics, 9, 0-24. https://doi.org/10. 1088/1367-2630/9/11/427
- Oriola, D., Needleman, D. J., & Brugués, J. (2018). The physics of the metaphase spindle. *Annual Review of Biophysics*, 47, 655–673.
- Peskin, C. S., Odell, G. M., & Oster, G. F. (1993). Cellular motions and thermal fluctuations: The brownian ratchet. *Biophysical Journal*, 65(1), 316–324.
- Plastino, J., & Sykes, C. (2005). The actin slingshot. Current Opinion in Cell Biology, 17(1), 62-66.
- Redemann, S., Baumgart, J., Lindow, N., Shelley, M., Nazockdast, E., Kratz, A., ... Müller-Reichert, T. (2017). C. elegans chromosomes connect to centrosomes by anchoring into the spindle network. Nature Communications, 8, 15288.
- Romero, S., Le Clainche, C., Didry, D., Egile, C., Pantaloni, D., & Carlier, M.-F. (2004). Formin is a processive motor that requires profilin to accelerate Actin assembly and associated atp hydrolysis. *Cell*, *119*(3), 419–429.

- Shelley, M. J. (2016). The dynamics of microtubule/motor-protein assemblies in biology and physics. Annual Review of Fluid Mechanics, 48, 487–506.
- Shimamoto, Y., Maeda, Y. T., Ishiwata, S., Libchaber, A. J., & Kapoor, T. M. (2011). Insights into the micromechanical properties of the metaphase spindle. *Cell*, 145(7), 1062–1074.
- Srayko, M., Kaya, A., Stamford, J., & Hyman, A. a. (2005). Identification and characterization of factors required for microtubule growth and nucleation in the early *C. elegans* embryo. *Dev. Cell*, *9*(2), 223–236. https://doi.org/10.1016/j.devcel.2005.07.003
- Stein, D. B., & Shelley, M. J. (2019). Coarse-graining the dynamics of immersed and driven fiber assemblies. *arXiv preprint arXiv*: 1902.00049.
- Strychalski, W., Copos, C. A., Lewis, O. L., & Guy, R. D. (2015). A poroelastic immersed boundary method with applications to cell biology. *Journal of Computational Physics*, 282, 77–97.
- Strychalski, W., & Guy, R. D. (2013). A computational model of bleb formation. *Mathematical Medicine and Biology: A Journal of the IMA*, 30(2), 115–130.
- Strychalski, W., & Guy, R. D. (2016). Intracellular pressure dynamics in blebbing cells. *Biophysical Journal*, 110(5), 1168–1179.

- Tornberg, A.-K., & Shelley, M. J. (2004, May). Simulating the dynamics and interactions of flexible fibers in stokes flows. *Journal of Computational Physics*, 196(1), 8–40.
- van Doorn, G. S., Tănase, C., Mulder, B. M., & Dogterom, M. (2000). On the stall force for growing microtubules. *European Biophysics Journal*, 29(1), 2–6.
- Wiens, J. K., & Stockie, J. M. (2015). Simulating flexible fiber suspensions using a scalable immersed boundary algorithm. *Computer Methods in Applied Mechanics and Engineering*, 290, 1–18.

# SUPPORTING INFORMATION

Additional supporting information may be found online in the Supporting Information section at the end of this article.

**How to cite this article:** Nazockdast E. Hydrodynamic interactions of filaments polymerizing against obstacles. *Cytoskeleton.* 2019;76:586–599. <a href="https://doi.org/10.1002/cm.21570">https://doi.org/10.1002/cm.21570</a>